JOURNAL OF FUEL CHEMISTRY AND TECHNOLOGY
Volume 54, Issue 2, February 2026

燃料化学学报(中英文)
Journal of Fuel Chemistry and Technology

Cite this article as: J Fuel Chem Technol, 2026, 54, 20250192

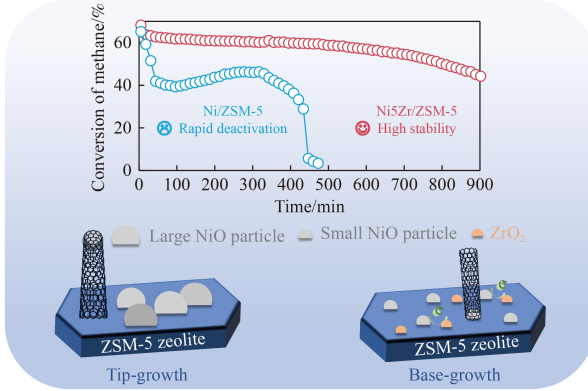
RESEARCH PAPER

The role of Zr in modulating the electronic and structural properties of supported Ni catalysts for catalytic decomposition of methane

LIU Lu, REN Shenyong*, YAO Chengshu, SHEN Baojian, XU Chunming

State Key Laboratory of Heavy Oil Processing, CNPC Key Laboratory of Catalysis, School of Chemical Engineering and Environmental Science, China University of Petroleum (Beijing), Beijing 102249, China

Abstract: Catalytic decomposition of methane, which produces high-purity hydrogen and high-value-added carbon nanomaterials, has shown considerable potential for development and is expected to yield significant economic benefits in the future. However, designing catalysts that simultaneously exhibit high activity and long-term stability remains a significant challenge. Tuning the catalyst's structure and electronic properties is an effective strategy for enhancing the reaction performance. In this work, a series of Ni*x*Zr/ZSM-5 catalysts were prepared using the incipient wetness impregnation method, and the effect of Zr loadings on catalyst properties and performance was systematically investigated. The calcined and reduced catalysts were characterized by low-temperature N_2 adsorption-desorption, XRD, SEM, H_2-TPR and XPS. The results showed that the addition of Zr significantly increased the specific surface area of the catalyst and reduced the metal particle size. Smaller NiO particles were found to enter the pores of the HZSM-5 support, and electronic interactions between NiO and ZrO_2 markedly enhanced the metal-support interaction. The catalyst exhibited optimal catalytic performance at a Zr loading of 5%, achieving a maximum methane conversion of 68% at 625 °C, maintaining activity for 900 min, and delivering a carbon yield of 1927%. Further increasing the Zr loading yielded only limited improvements in catalytic performance. Characterization of the spent catalysts and carbon products via TEM, Raman spectroscopy, and TGA revealed that the introduction of ZrO_2 reduced metal sintering and promoted a shift in carbon nanofibers growth mode from tip-growth to base-growth. The mechanism of base-growth enabled the catalyst to maintain reaction activity for an extended period.



Key words: promoter ZrO_2; Ni/HZSM-5; catalytic decomposition of methane; carbon nanofibers

Driven by global energy restructuring and the need to reduce carbon emissions, clean energy sources are attracting growing attention. Hydrogen, recognized as a clean energy carrier with abundant availability, high mass energy density, and high calorific value, is considered a sustainable alternative to fossil fuels[1]. Currently, steam methane reforming is the most widely used and mature industrial process for hydrogen production. However, this technology involves complex operations, produces carbon oxides (CO_x) emissions, and requires a hydrogen separation and purification process[2−3]. In contrast, catalytic decomposition of methane (CDM) produces high-purity hydrogen while concurrently yielding valuable carbon nanomaterials, which can be applied in fuel cells or advanced functional materials[4]. The CDM process offers a simple route and potential economic advantages. Notably, no CO_x emissions are generated during its reaction process, which consequently contributes to mitigating the greenhouse effect. Nevertheless, catalyst deactivation due to carbon deposition remains a persistent challenge, impeding the industrial application of CDM technology.

The highly symmetrical tetrahedral structure and high

Received: 2025-08-04; Revised: 2025-08-27
Foundation items: Supported by Innovative Research Groups of the National Natural Science Foundation of China (22021004).
* Corresponding author. Tel: 010-89732316, E-mail: shenyong@cup.edu.cn.
DOI: 10.1016/S1872-5813(25)60601-3 CSTR: 32157.14.2097-213X.2025.JFCT.0145
本文的英文电子版由 Elsevier 出版社在 ScienceDirect 上出版 (http://www.sciencedirect.com/science/journal/18725813)

C−H bond energy of methane make the thermal cracking of methane challenging. Thermodynamic analysis (Figure 1) reveals that the equilibrium conversion of methane remains low at conventional cracking temperatures. Therefore, catalysts are necessary to lower the activation energy to break the C−H bond[5]. Transition metal (Ni, Co, Fe) catalysts are extensively studied as CDM catalysts due to their low cost and excellent catalytic activity. Their activity stems from partially unfilled 3*d* orbitals in transition metals that accept electrons from C−H bonds of methane[6]. Ni-based catalysts exhibit high activity at lower reaction temperatures and are cost-effective. However, Ni metal readily undergoes sintering deactivation (>700 °C)[7]. To address this, researchers often employ strategies such as support or promoter modification to enhance the activity and stability of Ni-based catalysts.

The selection of the support plays a critical role in determining the reaction activity, stability, and structure of carbon products. Various supports have been applied in the preparation of CDM catalysts, including oxides (composite oxides), zeolites, layered double hydroxide, and perovskite materials[8]. Zeolites, which possess a unique pore structure and a tunable Si/Al ratio, facilitate the high dispersion of metal particles, making them ideal supports for CDM catalysts. Gutta et al.[9] significantly enhanced catalyst performance by using the high-surface-area MCM-41 support, which increased the interface between the active metal and the support. Yoon et al.[10] investigated how the positions of Ni particles relative to the zeolite pores affect Ni/SBA-15 catalysts. The results showed that Ni^0 particles confined within the zeolite pores had low carbon yield due to spatial restrictions and limited accessibility, while the carbon products exhibited high defect density. In previous studies, researchers have prepared the FeNi/HZSM-5 catalyst, which exhibited an initial methane conversion of 81.51% at 700 °C[11]. These findings confirm the viability of HZSM-5 as a CDM catalyst support. Nevertheless, the insufficient lifetime of the catalysts remains a key issue requiring immediate resolution.

The addition of promoters significantly impacts catalyst performance. Metal promoters can enhance the intrinsic activity of active sites[12], generate electronic synergistic effects with the active metal[13], or form alloys to modulate the crystal orientation and particle size of the active metal particles. Typically, the diffusion rate of carbon within metal promoters is higher than that of the active metal nickel[14−15], which can mitigate catalyst deactivation caused by the encapsulation of metal particles by carbon deposits. Furthermore, metal promoters can influence the strength of metal-support interaction (MSI) and modulate the reducibility of the catalysts[16]. Studies have indicated that adding Mn could enhance the activity, while adding Cu significantly improved the stability of nickel-based catalysts[17]. Iron (Fe) as a promoter, which alloys with Ni, can extend catalyst lifetime and promote the formation of bamboo-like carbon fibers[18]. LÜ et al.[19] synthesized a Ni-Zr catalyst via the citrate complexation method, achieving a methane conversion of 60% at 973 K with no activity decline over 4 h. Kosari et al.[20] also enhanced the uniform dispersion of Ni metal on the mSiO$_2$ support by doping a small amount of Zr. The catalyst exhibited good stability and cycling performance but low activity. The introduction of Zr is a promising strategy for enhancing the reaction stability of Ni-based catalysts. However, the interaction mechanisms among the Zr species, active metals, and supports require further investigation.

Catalyst deactivation due to carbon deposition remains a core challenge in the CDM process for hydrogen production. Balancing the methane molecular cracking rate, carbon deposition rate on catalyst surface, and carbon nanofibers (CNFs) growth rate is crucial for maintaining the activity and lifespan of catalysts[21]. Carbon products growth typically follows two mechanisms: tip-growth and base-growth. Literature has reported that Ni-based catalysts typically follow the tip-growth mechanism, where metal particles reside at the top of carbon filaments. Although the tip-growth mode can enhance activity, it also renders the catalysts prone to complete encapsulation by carbon filaments, leading to deactivation[22]. Consequently, researchers have introduced Mn to modulate the interactions between the metal and the support, thereby promoting a mode shift of carbon nanofibers from the tip-growth to the base-growth mode and significantly extending catalyst lifetime[23]. Introducing metal oxides to regulate the growth mechanism and morphology of carbon products is an effective strategy for enhancing catalyst stability as well as producing high-quality carbon nanomaterials.

This study employed HZSM-5 zeolite as the support and nickel as the active metal to prepare a series of ZrO_2-promoted NixZr/HZSM-5 catalysts via incipient wetness impregnation. The fresh and spent catalysts were characterized by XRD, H_2-TPR, NH_3-TPD, XPS, TGA, SEM and HRTEM. This investigation aims to clarify the mechanism by which promoter ZrO_2 modulates the electronic and structural properties of the catalysts, as well as its effect on CDM reaction performance. Furthermore, the correlation between the morphology and growth mode of the carbon nanofiber products, as well as their catalytic stability, was also investigated.

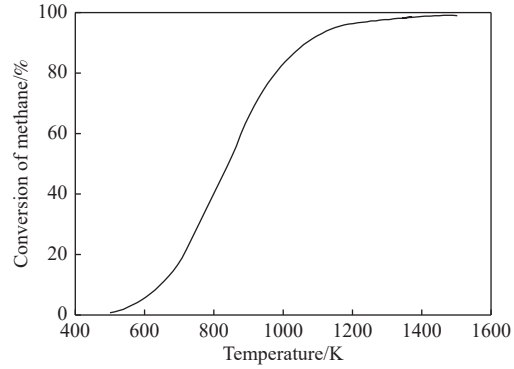


Fig. 1 Thermodynamic characteristics of catalytic decomposition of methane reaction[5]

1 Experimental

1.1 Catalyst synthesis

The HZSM-5 zeolite (SiO_2/Al_2O_3 molar ratio = 47) was purchased from the Nankai University Catalyst Co., Ltd. Nickel nitrate (($Ni(NO_3)_2{\cdot}6H_2O$, 98%, purchased from Shanghai Aladdin Bio-Chem Technology Co., Ltd.) and zirconium nitrate (($Zr(NO_3)_4{\cdot}5H_2O$, 98%, purchased from Beijing Inokai Technology Co., Ltd.) were used as metal precursors. Catalysts with a fixed Ni loading of 30% and varying Zr loadings of 3%, 5% and 7% were prepared via the incipient wetness impregnation method. First, an appropriate amount of metal nitrate was dissolved in deionized water under ultrasonication at 50 °C for 10 min to obtain a clear impregnation solution. The solution was then added dropwise to a measured quantity of HZSM-5 support placed in a crucible until the support was completely saturated. The impregnated samples were then aged at room temperature for 4 h to facilitate the uniform dispersion of the metal precursors within the support pores. Subsequently, the sample was dried at 120 °C overnight in an oven to remove moisture. The dried powder was thoroughly ground and calcined at 550 °C for 4 h in a muffle furnace under an air atmosphere, with a heating rate of 4 °C/min. The final catalysts were denoted as Ni*x*Zr/ZSM-5 catalysts (where *x* represents the Zr loading of 3%, 5% or 7%). For comparison, the Ni/ZSM-5 catalyst with 30% Ni was prepared following the same procedure. All catalysts were pelletized, crushed, and sieved to 40−60 mesh for catalytic evaluation in the catalytic decomposition of methane reaction.

1.2 Catalyst characterizations

The elemental composition of the samples was analyzed using a Thermo iCAP PRO X inductively coupled plasma emission spectrometer. The textural properties of the samples were characterized by N_2 physisorption at 77 K using a Micromeritics TriSTAR II 3020 analyzer. The specific surface area was calculated using the BET method, the pore size distribution curve was obtained via the BJH method, and the micropore specific surface area and pore volume were determined using the *t*-plot method. Phase analysis of calcined, reduced, and spent catalysts was performed using X-ray powder diffraction (XRD) with a PANalytical X'Pert Powder XRD instrument. The crystallite size (d) of metal and metal oxide phases was estimated using the Scherrer equation: ($d = 0.9\lambda/(\beta \times \cos\theta)$), where λ is the X-ray wavelength, β is the full width at half maximum (FWHM), and θ is the Bragg angle. FT-IR spectroscopy analysis of calcined and reduced samples was performed using a Thermo Fisher Nicolet IS10 spectrometer. The morphology and size distribution of the catalysts before and after reaction were examined using a ZEISS GeminiSEM 300 field-emission scanning electron microscope (FE-SEM). The acid properties (NH_3-TPD) and reduction properties (H_2-TPR) of all catalysts were characterized using a Micromeritics AutoChem II 2920 chemisorption analyzer. The surface composition and chemical valence states of the samples were characterized using a Thermo Fisher *K*-Alpha X-ray photoelectron spectrometer. The microstructure of the carbon products and the location of metal particles were characterized using a JEOL JEM-2100 high-resolution transmission electron microscope (HRTEM). Thermogravimetric analysis (TGA) of spent catalysts was conducted under an O_2 atmosphere using a Simultaneous DSC-TGA Q600 instrument. The graphitization degree of carbon products was characterized by Raman spectroscopy using a Horiba Jobin Yvon T6400 Raman spectrometer.

1.3 Catalyst evaluation

The catalytic decomposition of methane reaction was conducted in an atmospheric fixed-bed stainless steel reactor with an inner diameter of 8 mm and a length of 400 mm. Typically, 0.1 g of catalyst was loaded into the isothermal zone of the reaction tube. Under a 20 mL/min N_2 atmosphere, the reactor was heated to 400 °C at a rate of 10 ℃/min. Then, the feed gases of 2.5 mL/min N_2 and 7.5 mL/min CH_4 were introduced to analyze the composition by gas chromatography at this temperature. The reactor was next purged with 20 mL/min N_2 for 30 min while raising the temperature to 550 °C. The gas stream was then switched to 10 mL/min H_2 for 120 min to pre-reduce the catalyst. Then 20 mL/min N_2 was purged to the reaction tube until no residual H_2 was detected, and the system was heated to the reaction temperature of 625 °C. The gas was switched to a mixture of 2.5 mL/min N_2 and 7.5 mL/min CH_4 to initiate the reaction. After a stabilization time of 5 min, the composition of the outlet gas (containing only H_2, N_2 and CH_4) was analyzed online by gas chromatography. Following reaction completion, the spent catalyst and carbon products were collected and weighed. The effluent gas was analyzed using an Agilent GC 8890 gas chromatograph equipped with a thermal conductivity detector (TCD) and a 13X molecular sieve column. Gas quantification was performed using the internal standard method, with N_2 serving as the internal standard since it is inert in the CDM reaction. Prior to reaction tests, the GC was calibrated using standard mixtures of H_2, N_2 and CH_4 with known concentrations to establish the calibration factors for each component. The known flow rate of N_2 in the feed was used to calculate the volumetric flow rate of the outlet stream ($F_{CH_4,out}$). Catalyst performance was evaluated by calculating the methane conversion, carbon yield, and catalyst deactivation factor (*DF*), using the following equations:

$$\text{CH}_4\ \text{conversion}(\%): x_{CH_4} = \frac{F_{CH_4,in} - F_{CH_4,out}}{F_{CH_4,in}} \times 100\% \quad (1)$$

$$\text{Carbon yield}(\%): Y_C = \frac{M_C}{M_{cat}} \times 100\% \quad (2)$$

$$\text{Deactivation factor}(\%): DF = \frac{x_0 - x_t}{x_0} \times 100\% \quad (3)$$

In the equation, $F_{CH_4,in}$ and $F_{CH_4,out}$ represent the methane gas flow rate in the feedstock and product gases, respectively. M_C denotes the mass of carbon product, M_{cat} represents the mass of catalyst, x_0 and x_t denote the initial methane conversion and the methane conversion at t minute, respectively.

2 Results and discussion

2.1 Structural and acidic properties characterization of catalysts

Inductively Coupled Plasma-Optical Emission Spectroscopy (ICP-OES) analysis indicated that the actual loadings of Ni and Zr in the catalysts were consistent with the theoretical values (Table 1), suggesting negligible metal loss during the impregnation process. The textural properties of the support and calcined catalysts were evaluated using low-temperature N_2 physisorption-desorption measurements. As depicted in Figure 2(a), the pure HZSM-5 support displayed a Type I adsorption isotherm, which is typical of microporous zeolite materials. As shown in Figure 2(b), a distinct pore size distribution below 2 nm was observed. After metal loading, all catalysts exhibited Type IV isotherms with H4-type hysteresis loops, characteristic of slit-like mesoporous structures. The mesopores likely originated from the stacking of metal oxide particles, which block the micropores of the support[24]. The textural data of the support and catalysts are listed in Table 1. The BET surface area of the HZSM-5 support was 282 m^2/g. This high surface area and microporous structure are favorable for high metal dispersion and facilitate gas diffusion. After loading 30% Ni, the S_{BET} of the Ni/ZSM-5 catalyst decreased significantly, suggesting the aggregation of NiO on the support surface. The Ni3Zr/ZSM-5 catalyst exhibited a lower BET surface area, which may result from the elevated total metal loading. However, as the Zr loading increased to 5% and 7%, the specific surface area of the catalyst gradually increased. This phenomenon is likely due to the higher ZrO_2 loading promoted NiO dispersion, effectively inhibiting the sintering and growth of NiO particles during calcination and thereby reducing the blockage of support pores by larger NiO particles. Concurrently, increasing Zr loading increased the total pore volume while decreasing the average pore diameter of the catalysts. This indicates that the introduction of ZrO_2 may be distributed within smaller pores or embedded in the inner walls of support pores, thus reducing the pore size[10]. These alterations in the textural properties are expected to significantly influence the catalytic reactivity and stability in the CDM reaction.

Figure 3(a) presents the XRD patterns of the calcined catalysts. All catalysts exhibited characteristic peaks corresponding to the MFI structure of the HZSM-5 zeolite at 2θ = 7°–9° and 23°–25°[25], indicating that the impregnation process did not destroy the crystalline structure of the support. Additionally, prominent diffraction peaks were observed at 2θ = 37.3°, 43.4°, 63.0°, 75.6° and 79.2°, which are assigned to the NiO phase. Due to the low content and high dispersion of the ZrO_2, its characteristic peak at 2θ = 30.1° was masked by the diffraction peaks of the HZSM-5 support[26]. With the introduction of Zr, the increased intensity and broadened FWHM of the NiO peaks suggest improved metal dispersion and a reduction in crystallite size. The average crystallite sizes of NiO in the calcined catalysts calculated using the Scherrer equation are listed in Table 1. The NiO crystallite sizes followed the order: Ni/ZSM-5 > Ni3Zr/ZSM-5 > Ni5Zr/ZSM-5 > Ni7Zr/ZSM-5, confirming that the crystallite size decreased with increasing Zr loading.

Figure 3(b) shows the XRD patterns of the reduced catalysts. After the H_2 pre-reduction process, the characteristic peaks of NiO were no longer detectable. The characteristic peaks of the Ni^0 phase appeared at approximately 2θ = 44.5°, 51.8°, and 76.4°, which are assigned to the (111), (200) and (220) crystal planes of metallic Ni (Ni^0), respectively[27]. This confirms that the Ni oxides were effectively reduced to Ni^0. With the increase in ZrO_2 content, the intensity of the Ni^0 diffraction peaks decreased significantly and the FWHM broadened, demonstrating that the ZrO_2 promoter exerts a significant inhibitory effect on the growth of Ni^0 on the catalyst surface.

Table 1 Physical and chemical properties of different catalysts

Sample	ICP		S_{BET} /($m^2 \cdot g^{-1}$)	v_t /($cm^3 \cdot g^{-1}$)	Average pore size/nm	Crystallite size[a] d/nm		Total acid density[b] /(μmol·g^{-1})
	Ni/%	Zr/%				calcined	reduced	
ZSM-5	–	–	282	0.143	4.5	–	–	229
Ni/ZSM-5	31.2	0.0	165	0.096	45.2	36.5	66.5	239
Ni3Zr/ZSM-5	29.4	3.1	140	0.109	23.4	34.2	40.6	257
Ni5Zr/ZSM-5	28.7	4.9	154	0.142	15.0	29.4	33.9	250
Ni7Zr/ZSM-5	25.8	6.8	173	0.149	13.6	24.0	28.1	238

[a]: The average crystallite sizes of NiO and Ni^0 were calculated using the Scherrer equation; [b]: The total acidity of the support and catalysts was calculated via NH_3-TPD.

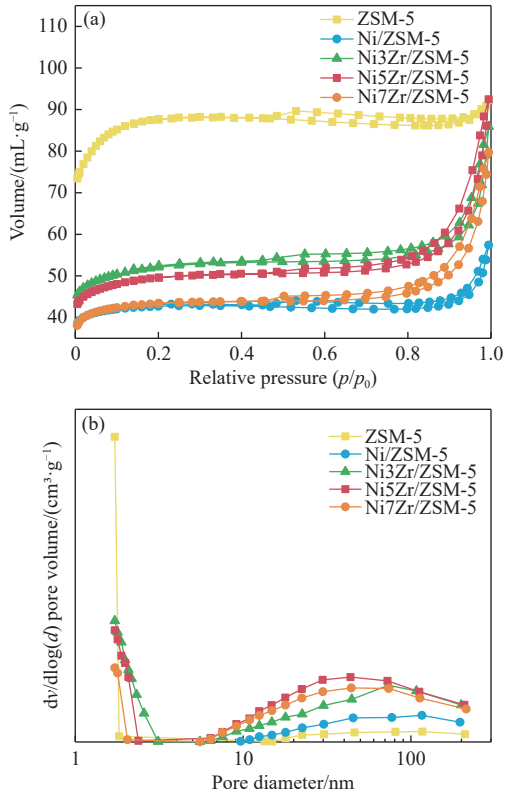


Fig. 2 (a) N_2 adsorption-desorption isotherms and (b) BJH pore size distributions of the support and catalysts

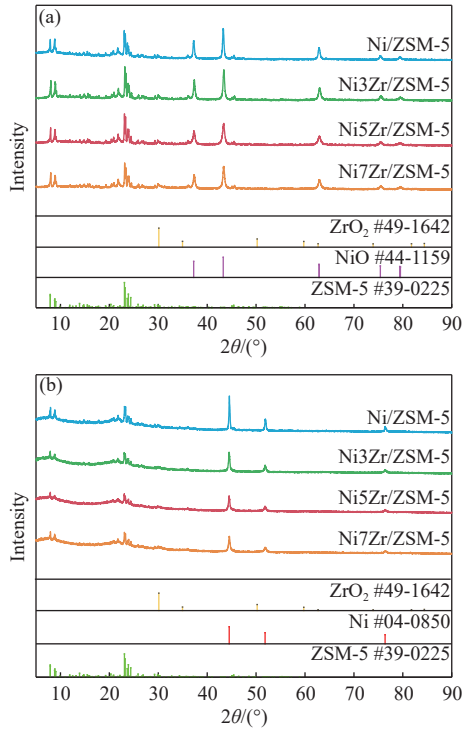


Fig. 3 XRD patterns of (a) calcined and (b) reduced catalysts

It is conducive to the dispersion of active metals, thereby enhancing the catalytic reactivity and stability. Crystallite size also affects the type of reactively deposited carbon, which is consistent with the SEM characterization results of carbon products formed over different catalysts. The average crystallite size of Ni^0 exhibited a notable increase compared with NiO, which is attributed to crystallite growth and agglomeration induced by high-temperature reduction. The dispersion degree (D) of Ni^0 on the support surface can be reflected by the formula: $D=K/d(Ni^0)$[28], where K is a constant and d represents crystallite size. With the increase in ZrO_2 loading, the average crystallite size of Ni^0 decreased from 66.5 to 28.1 nm, indicating a significant improvement in metal dispersion. This observation can be ascribed to the strong interaction between the promoter ZrO_2 and Ni^0 species on the catalyst, which restricts the growth of Ni particles. Such a restriction is beneficial for enhancing the utilization efficiency of active Ni species and suppressing the agglomeration and sintering of Ni particles during the CDM reaction.

Figure 4(a)−(d) presents the SEM images of the calcined catalysts. All catalysts consist of nanoparticles stacked on the support, confirming the successful loading of the metal oxides. As the ZrO_2 loading increases, particle agglomeration decreases, leading to a reduction in the average particle size. This trend indicates an improved dispersion of the metal oxide particles on the HZSM-5 support.

Figure 5(a) and (b) present the Fourier transform infrared (FT-IR) spectra of the calcined and reduced catalysts, providing information on their chemical bonding. The spectra reveal that both calcined and reduced catalysts exhibit typical characteristic vibrational bands of the MFI structure. Specifically, the absorption bands near 452 cm^{-1} (Si−O bending vibration), 797 cm^{-1} (external symmetric stretching), 1100 cm^{-1} (internal asymmetric stretching) and 1220 cm^{-1} (external asymmetric stretching) correspond to the vibrations of Si−O−Si bonds in the HZSM-5 support. The absorption band at 547 cm^{-1} is attributed to the five-membered ring unit in the MFI structure[29]. These results clearly indicate that neither the loading of NiO and ZrO_2 nor the high-temperature reduction process disrupted the framework structure of the ZSM-5 zeolite. Furthermore, the absorption band at 1103 cm^{-1} of the Ni/ZSM-5 catalyst is broadened. NiO particles may be embedded in the zeolite channels, which induce localized framework stress. In contrast, the ZrO_2-promoted catalysts exhibit absorption bands nearly identical to those of the pure HZSM-5 support. This observation suggests that the introduction of ZrO_2 may promote the dispersion or alter the site occupancy of Ni species. Consequently, the local disturbances and structural damage to the ZSM-5 framework caused by high Ni loading are mitigated.

The acidity of the catalyst also influences its catalytic performance in the CDM reaction. Accordingly, the acid properties of the HZSM-5 support and all catalysts were characterized by ammonia temperature-programmed desorption (NH_3-TPD). As shown in Figure 5(c), all samples exhibited two distinct desorption peaks in the temperature ranges of 50−250 and 250−500 °C, corresponding to weak and strong acid sites, respectively[30].

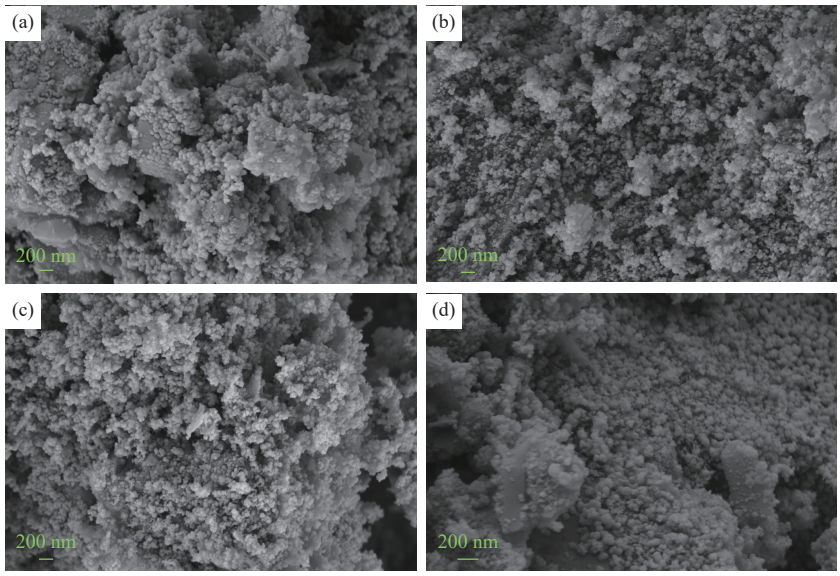


Fig. 4 SEM images of calcined catalysts ((a) Ni/ZSM-5, (b) Ni3Zr/ZSM-5, (c) Ni5Zr/ZSM-5, (d) Ni7Zr/ZSM-5)

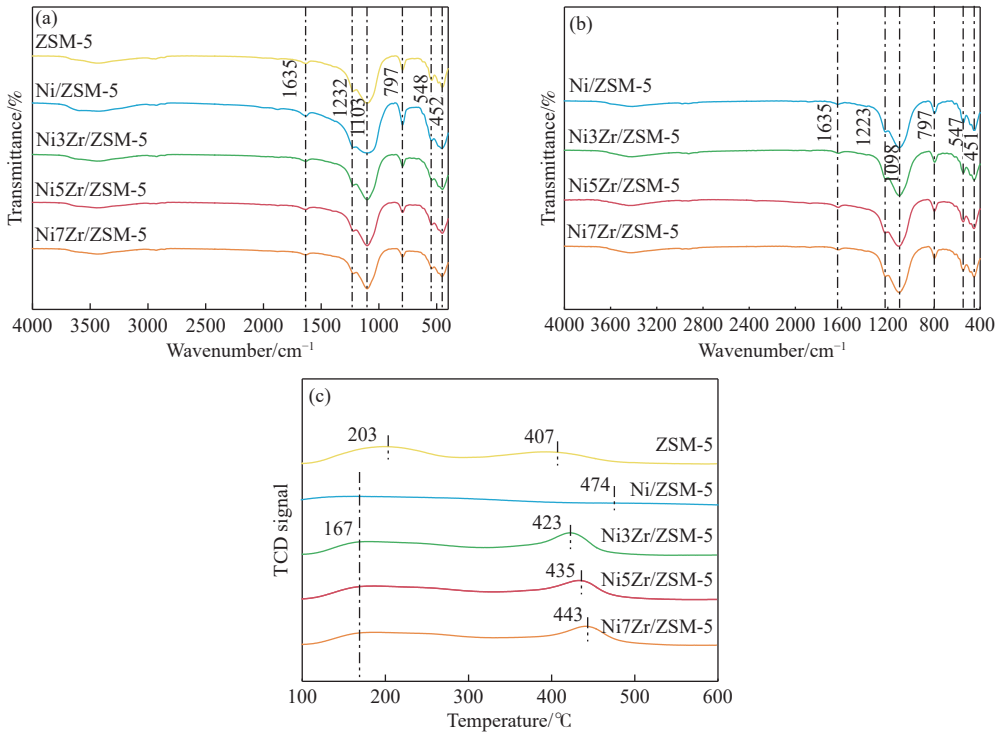


Fig. 5 FT-IR spectra of (a) calcined, (b) reduced catalysts and (c) NH_3-TPD profiles of calcined catalysts

After loading with NiO, the weak acid peak shifted to lower temperatures, indicating a decrease in weak acid strength, while the strong acid peak shifted to higher temperatures, suggesting enhanced strength. Further loading with ZrO_2 left the weak acid peak temperature largely unchanged. For all Ni*x*Zr/ZSM-5 catalysts, the strong acid peak temperature decreased while its intensity increased significantly. This indicates an increase in the number of strong acid sites but a reduction in their acid strength. However, the strong acid peak temperature increased slightly with higher Zr loading, indicating a recovery of strong acid strength. As summarized in Table 1, the total acidity of the catalyst increased after NiO loading. With increasing Zr loading, the total acidity first increased (Ni3Zr/ZSM-5 catalyst exhibited the maximum of 257 μmol/g), and then gradually decreased. This trend is attributed to the introduction of new Lewis acid sites by the loaded NiO and ZrO_2. Optimal strong acid strength and total acidity are conducive to the CDM reaction, improving coke resistance and achieving higher catalytic stability[11].

2.2 Effect of Zr species on the metal-support interaction of catalysts

The metal-support interaction and reducibility of Ni/ZSM-5 catalysts with different Zr loadings were investigated by H_2 temperature-programmed reduction (H_2-TPR), and the corresponding profiles are presented in Figure 6(a). The location of the reduction peaks is determined by the particle size of NiO, the pore size of the HZSM-5 support, and the interaction between NiO particles and HZSM-5 support. As shown in Figure 6(a), all catalysts exhibit two distinct H_2 consumption peaks in the temperature ranges of 300−400 and 400−500 °C, denoted as the peak α and peak β. According to the literature, the reduction peak at the lower temperature (peak α) is attributed to the reduction of free NiO species located on the external surface of the support. In contrast, NiO particles with smaller sizes or NiO species encapsulated within the support channels form a strong interaction with the support. This strong interaction increases the difficulty of reduction, thus leading to the appearance of the H_2 consumption peak (peak β) at a higher temperature[23].

The Ni/ZSM-5 catalyst exhibited the lowest reduction temperatures of peak α and β at 343 and 438 °C, respectively. Notably, peak α accounted for the largest area (98%) of the total consumption. This indicates that larger NiO particles are predominantly distributed on the surface of HZSM-5 support, exhibiting a weaker MSI. Increasing the loading of Zr, both peak α and peak β shifted significantly toward higher temperatures, indicating enhanced interactions between the NiO species inside and outside the support pores and the support. The Ni5Zr/ZSM-5 catalyst exhibited the highest reduction temperature. However, when the Zr loading was increased to 7%, both reduction peaks shifted toward lower temperatures, occurring at 367 and 466 °C, respectively, though still higher than those of the Ni/ZSM-5 and Ni3Zr/ZSM-5 catalysts. Strong metal-support interaction (SMSI) can reduce Ni particle aggregation by limiting Ni metal migration and growth on the support, promoting dispersion and enhancing catalyst stability[31]. Furthermore, after the introduction of Zr, the relative area proportion of the peak α decreased while that of the peak β increased significantly (Figure 6(b)). This observation indicates that the incorporation of Zr exerts a notable effect on both the particle size of NiO and the distribution of NiO species within the support channels. NiO species with small crystallite sizes and SMSI can maintain their activity over both low and high temperature ranges. Furthermore, these species exhibit resistance to metal sintering during the reduction process, which is conducive to enhancing the catalytic stability of the catalyst. To better understand the influence of Zr species on catalyst reducibility, the total H_2 consumption and reduction degree for different catalysts are listed in Table 2. The Ni5Zr/ZSM-5 catalyst exhibited the highest H_2 consumption (4.8 mmol/g) and reduction degree (99%). This indicates that the maximum amount of Ni^0 species was formed during the reduction process, which implies more active sites on the catalyst surface.

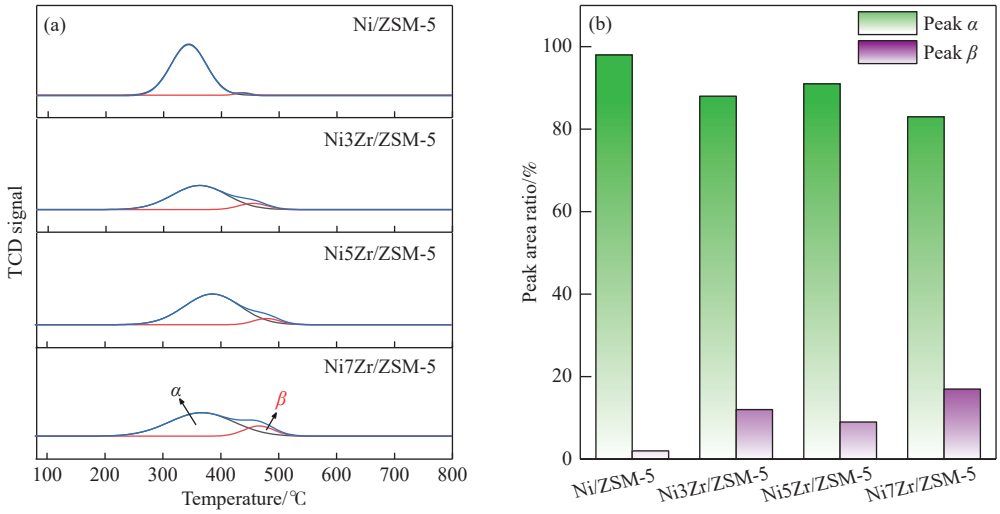


Fig. 6 (a) H_2-TPR curves and (b) peak area ratio of different catalysts

Table 2 Analysis of H_2-TPR of different catalysts results and *DF* values of CDM reaction

Sample	Peak α/℃	Peak β/℃	H_2 consumption /(mmol·g^{-1})	Reduction degree /%	*DF*/%			
					200 min	473 min	800 min	1032 min
Ni/ZSM-5	343	438	4.7	88	33	95	–	–
Ni3Zr/ZSM-5	362	455	4.8	95	9	21	95	–
Ni5Zr/ZSM-5	386	479	4.8	99	11	13	26	97
Ni7Zr/ZSM-5	367	466	4.3	97	8	14	26	90

X-ray photoelectron spectroscopy (XPS) was employed to characterize the surface composition and chemical states of the catalysts. Figure 7(a) presents the high-resolution Ni 2*p* XPS spectra of the calcined Ni/ZSM-5 and Ni5Zr/ZSM-5 catalysts. Both catalysts exhibit the peaks of Ni^{2+} $2p_{1/2}$ and Ni^{2+} $2p_{3/2}$, along with their corresponding satellite peaks. Compared with the Ni/ZSM-5 catalyst, the binding energies of the Ni^{2+} $2p_{1/2}$ and Ni^{2+} $2p_{3/2}$ peaks of the Ni5Zr/ZSM-5 catalyst shift to higher values by 1.4 and 0.6 eV, respectively. This shift indicates a decrease in the electron density around Ni atoms. The introduced Zr^{4+} species withdraws electrons from Ni through the formation of Ni−O−Zr interfacial bonds, generating an electron transfer effect. This effect enhances the MSI, which is consistent with the observation in the H_2-TPR profiles that the reduction peaks shift toward the higher temperature region.

High-resolution Ni 2*p* and Zr 3*d* XPS spectra of the reduced Ni5Zr/ZSM-5 catalyst are shown in Figure 7(b) and (c). The binding energies of the Ni^{2+} peaks remained essentially unchanged compared to those in the calcined catalyst. However, the reduced catalyst exhibited Ni^0 $2p_{1/2}$ and Ni^0 $2p_{3/2}$ peaks at 871.8 and 852.8 eV, respectively, confirming the successful reduction of NiO. The persistence of Ni^{2+} is attributed to the strong interaction formed between some small NiO particles and the support, which hinders their complete reduction. In the Zr 3*d* XPS spectrum, the peaks at 184.6 and 182.2 eV are assigned to the $3d_{3/2}$ and $3d_{5/2}$ orbitals of ZrO_2 species[32], which further confirms the oxide state of Zr after the reduction process.

The strong electronic interaction between the ZrO_2 support and Ni species effectively inhibits the agglomeration of NiO particles, as well as the sintering of Ni^0 particles formed after reduction. Furthermore, this interaction modifies the distribution of NiO species, promoting the migration of smaller particles into the channels of the HZSM-5 support, thereby forming a stronger interaction with the support. Optimal metal-support interaction and high Ni dispersion are crucial for the efficient and stable catalytic activity of the Ni5Zr/ZSM-5 and Ni7Zr/ZSM-5 catalysts.

2.3 Catalyst performance test

To analyze and compare the catalytic activity and stability of the prepared catalysts, the catalytic decomposition of methane reaction was evaluated over the reduced catalysts under a reaction temperature of 625 °C and a gas hourly space velocity (GHSV) of 6000 mL/(h·g). Figure 8(a) presents the curves of methane conversion versus time for different catalysts. As shown in the curves, the introduction of ZrO_2 as a promoter significantly enhances catalyst stability. Although all promoted catalysts with different Zr loadings exhibited comparable initial methane conversions (65%−70%), their operational lifetimes differed significantly. Compared with the Ni/ZSM-5 catalyst without Zr loading, the lifetimes of the Ni5Zr/ZSM-5 and Ni7Zr/ZSM-5 catalysts are prolonged by more than a factor of two. The deactivation factor *DF* values of both catalysts are only 26% at 800 min. However, when the reaction proceeds to 1032 min, the *DF* values of the two catalysts exceed 90% (Table 2), indicating almost complete deactivation. The unpromoted Ni/ZSM-5 catalyst suffered from large NiO crystallites due to the high Ni loading. After the reduction process, the Ni crystallite size increases significantly to 66.5 nm, which makes the catalyst more prone to sintering during the high-temperature reaction.

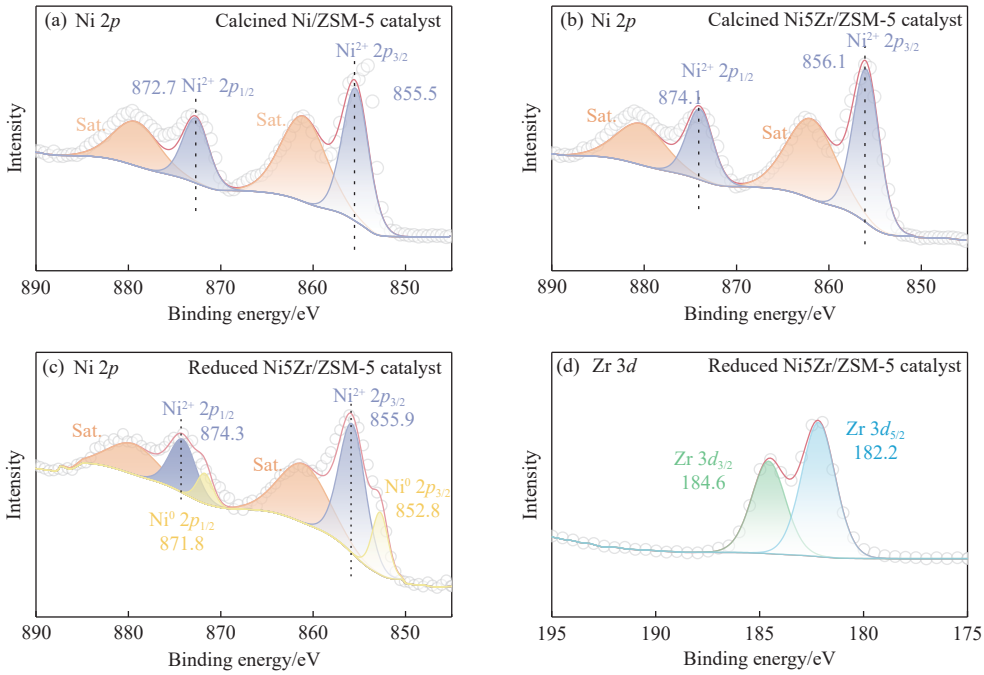


Fig. 7 High-resolution Ni 2*p* XPS spectra of calcined (a) Ni/ZSM-5 and (b) Ni5Zr/ZSM-5 catalyst, high-resolution (c) Ni 2*p* and (d) Zr 3*d* XPS spectra of reduced Ni5Zr/ZSM-5 catalyst

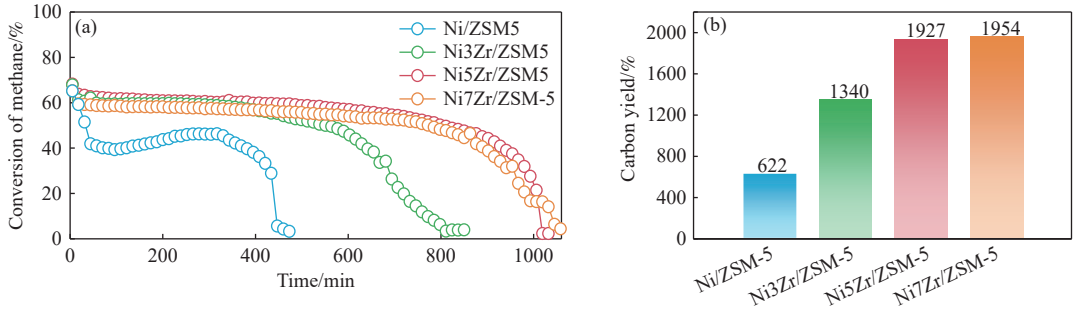


Fig. 8 (a) CH_4 conversion with time on steam and (b) carbon yield of different catalysts

Severe sintering and coking led to a rapid deactivation of Ni/ZSM-5 after only 400 min. When ZrO_2 was introduced as a promoter with different loadings, all catalysts' lifetimes significantly improved. The stability increased to over 600 min at a Zr loading of 3% while the Ni5Zr/ZSM-5 catalyst achieved over 900 min. Upon further increasing the Zr loading to 7%, the CDM reaction stability was essentially consistent with that of the Ni5Zr/ZSM-5 catalyst. These results indicate that increasing the Zr loading can significantly enhance the catalyst stability; however, the improvement becomes limited once the Zr loading reaches a certain threshold. The promoter ZrO_2 enhances the interaction between the support and Ni species, which inhibits the crystallite growth and agglomeration of NiO precursors during the calcination process. This, in turn, improves the dispersion of active sites Ni^0 after reduction and effectively enhances the catalyst's sintering resistance. Furthermore, the incorporation of ZrO_2 modulates the acidity of the catalysts. An optimal balance of total acidity and strong acid strength is beneficial for delaying the catalyst deactivation caused by coking.

As shown in Figure 8(b), the carbon yiled varied significantly among the tested catalysts. While the unpromoted Ni/ZSM-5 catalyst yielded only 622% carbon, the promoted Ni5Zr/ZSM-5 and Ni7Zr/ZSM-5 catalysts both exhibited a more than threefold increase, reaching 1927% and 1954%, respectively. This remarkable improvement in carbon production is consistent with the high activity stability in the CDM reaction.

2.4 Characterization of spent catalysts

The crystal structures of the spent catalysts were analyzed using X-ray diffraction (XRD), with the XRD patterns shown in Figure 9(a). A prominent diffraction peak corresponding to the (002) crystal plane of graphitic carbon was observed at 2θ = 26.1° for all spent catalysts[33]. Meanwhile, characteristic peaks of the (111), (200) and (220) crystal planes of Ni^0 phase were detectable at 2θ = 44.3°, 51.7° and 76.3°, respectively. Additionally, weak diffraction peaks of the ZSM-5 zeolite support and amorphous carbon (2θ = 29.7° and 42.5°) were observed. With the increase of Zr content, the diffraction intensities of the support and Ni^0 gradually decreased, whereas the intensity of the graphitic carbon (002) peak increased progressively. The XRD patterns revealed that the Ni/ZSM-5 catalyst contained the highest amount of residual deactivated Ni species. This is attributed to the rapid deactivation of larger Ni particles at high temperature and the encapsulation of active sites by carbon deposits, which hinders reactant access. Its shorter catalyst lifetime also resulted in the lowest accumulation of carbon products. Upon incorporating ZrO_2 into the catalyst, the catalyst lifetime was significantly extended, and the amount of unreacted Ni species decreased gradually. This suggests that the encapsulation of active sites by deposited carbon and metal sintering was inhibited, possibly due to the restriction of Ni grain growth by ZrO_2 and the altered growth mechanism of carbon nanotube products. Consequently, the Ni7Zr/ZSM-5 catalyst exhibited the highest diffraction intensity of graphitic carbon, which is consistent with its long lifespan and highest yield of carbon products.

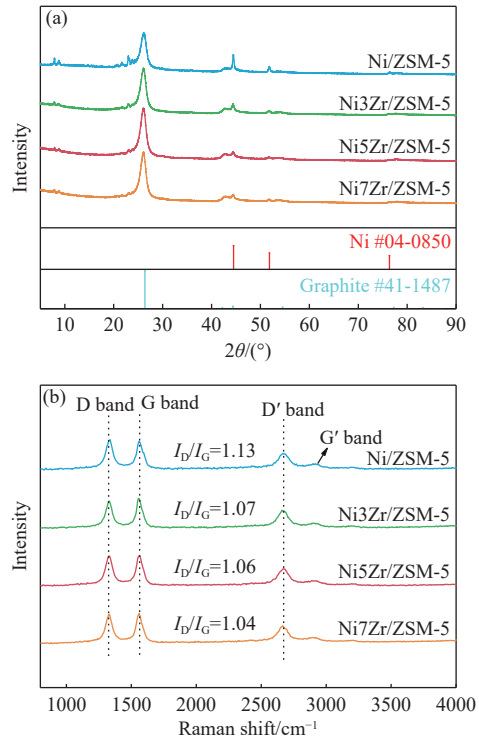


Fig. 9 (a) XRD patterns and (b) Raman spectra of the spent catalysts

Raman spectroscopy was employed to investigate the graphitization degree of carbon products formed on different catalysts after CDM reaction at 625 °C. As shown in Figure 9(b), all the spent catalysts exhibit four characteristic bands. The band near 1340 cm^{-1} corresponds to the D band, attributed to disordered carbon species with sp^3-hybridized carbon atoms. The band near 1590 cm^{-1} corresponds to the G band, attributed to sp^2-hybridized carbon atoms within the ordered graphitic phase lattice[34]. The second-order bands (labeled as D′ and G′ bands at 2655 and 2910 cm^{-1}, respectively) represent two-phonon scattering processes. The relatively low intensities of the D′ and G′ bands indicate the formation of a small amount of graphene flakes[35]. The degree of graphitization of carbon materials can be reflected by the peak area ratio of the D band to the G band (I_D/I_G). A higher value of I_D/I_G indicates more defects in the carbon products and a lower degree of graphitization[36]. The spent Ni/ZSM-5 catalyst exhibited the highest I_D/I_G value of 1.13, consistent with SEM observations showing predominantly coarse carbon nanofibers alongside abundant disordered spherical carbon and metal agglomerates. As the Zr loading increased, the I_D/I_G value of the spent Ni*x*Zr/ZSM-5 catalysts decreased. The spent Ni7Zr/ZSM-5 catalyst exhibited the lowest I_D/I_G value of 1.04, indicating a more ordered structure and the highest degree of graphitization of the carbon products. The deposition of disordered carbon is more prone to encapsulate the catalyst surface, thereby blocking the active sites and terminating the catalytic reaction, which constitutes a major deactivation mechanism. This conclusion aligns with the catalytic evaluation results, wherein the Ni7Zr/ZSM-5 catalyst demonstrated the longest lifetime at a similar methane conversion level compared to the other catalysts.

Scanning electron microscopy (SEM) was employed to characterize the morphology of carbon deposits formed on the catalysts, as presented in Figure 10. After the reaction, the surface of all catalysts was covered with a large quantity of carbon nanofibers; however, the incorporation of Zr significantly influenced the morphology and average diameter of the carbon products. The carbon products on the spent Ni/ZSM-5 and Ni5Zr/ZSM-5 catalysts exhibited similar morphologies, mostly consisting of relatively thick and short whisker-like CNFs (Figure 10(a), (c)). Spherical carbon and sintered metals were observed on the spent Ni/ZSM-5 catalyst, which may account for its short reaction lifespan. In contrast, the Ni3Zr/ZSM-5 and Ni7Zr/ZSM-5 catalysts generated longer and entangled CNFs (Figure 10 (b), (d)). The diameter distribution of CNFs produced by different catalysts was statistically analyzed using the Nano Measure software, and the order of average diameters was determined as follows: Ni5Zr/ZSM-5 (96.7 nm) > Ni7Zr/ZSM-5 (92.5 nm) > Ni/ZSM-5 (88.4 nm) > Ni3Zr/ZSM-5 (86.1 nm). This result indicates that the average diameter of CNFs increased with the extension of reaction time. During the CDM reaction, the migration of active metals and encapsulation of carbon as the reaction proceeds may affect both the catalyst stability and the growth mechanism of CNFs. From the SEM images, it can be observed that all CNFs grown on the catalysts exhibit an obvious open end. The growth mode of CNFs can be inferred by observing the distribution position of metals at the opposite end.

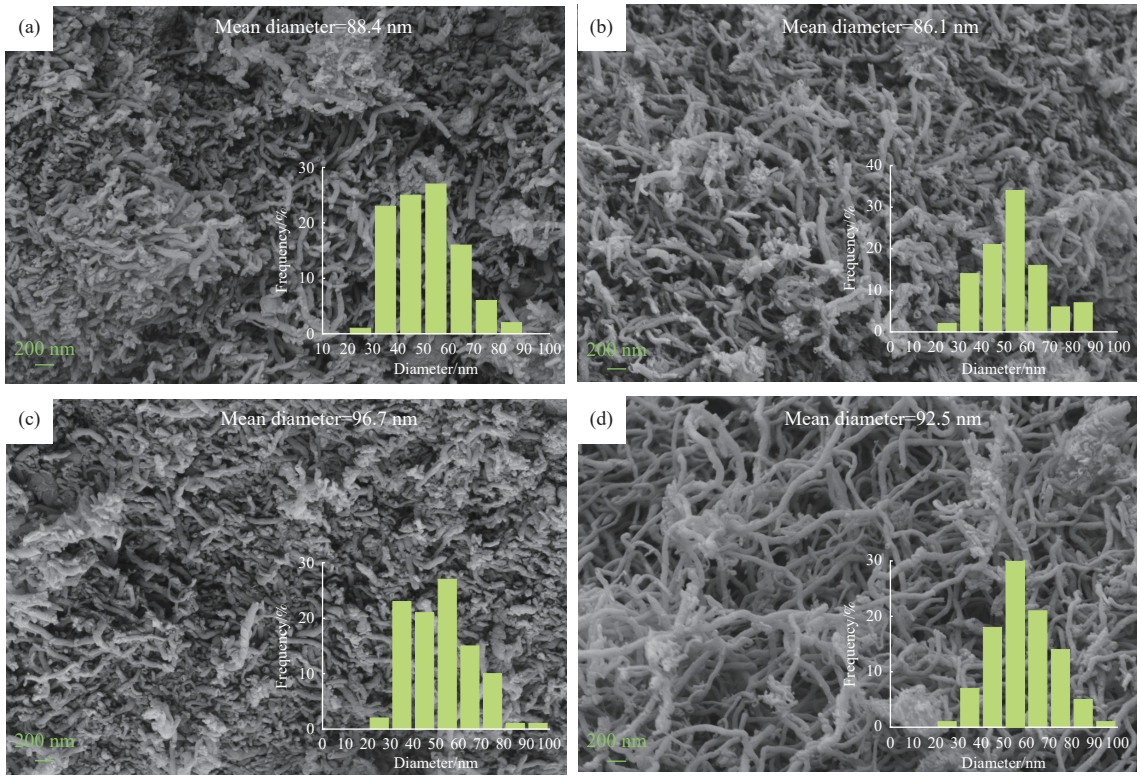


Fig. 10 SEM images of different catalysts after reaction

Transmission electron microscopy (TEM) analysis was further conducted to investigate the morphology of carbon products and the distribution of metal grains on the Ni/ZSM-5 catalyst and the Ni7Zr/ZSM-5 catalyst. As shown in Figure 11(a), (b), the carbon products formed on the Ni/ZSM-5 catalyst after reaction include thicker carbon nanofibers, carbon nanotubes (CNTs) with metal particles at their tips, and spherical carbon encapsulating metal particles. This indicates that the growth of carbon products follows the tip-growth mode[37]. The diagonal length of the conical Ni particles at the tips reached 176.5 nm, which is much larger than the size of the Ni^0 particles of the reduced catalyst. This confirms that Ni metal undergoes agglomeration and reconstruction during the CDM reaction[27], leading to the rapid deactivation of the catalyst. In contrast, CNFs with one end open and almost no metal particles distributed at the tips were observed in Figure 11(f), (g) of the spent Ni7Zr/ZSM-5 catalyst, indicating a base-growth mode. The introduction of ZrO_2 can regulate the rate of CH_4 dissociation and the rate of carbon diffusion, thereby stabilizing the growth of CNFs. Meanwhile, the introduction of Zr enhanced the MSI, promoting the transformation of the growth mechanism of the carbon products from the tip-growth mode to the base-growth mode. This transformation prevents the active sites of the catalyst from being damaged by carbon encapsulation[20]. As presented in Figure 11(h), the size of Ni^0 particles embedded in the CNFs is approximately 10 nm, which is much smaller than the size of Ni^0 grains after H_2 reduction. The fragmentation and dispersion of Ni grains are presumably responsible for the high activity and long lifespan during the CDM reaction.

Thermogravimetric analysis (TGA) of spent catalysts was performed to characterize the thermal stability and oxidation behavior of the carbon products. As presented in Figure 12(a), a slight weight loss is observed in the TG curve within the temperature range of 300−400 °C, which is attributed to the combustion of amorphous carbon. This was followed by a major weight loss, corresponding to the combustion of graphitic carbon. All the spent catalysts exhibited a primary, single-stage oxidation process between the temperatures of 550 and 650 °C. This result indicates that the carbon deposited on the surface of Ni/ZSM-5 and Ni*x*Zr/ZSM-5 consists primarily of high-purity carbon nanofibers[38]. The total weight loss for the spent catalysts decreased in the order: Ni7Zr/ZSM-5 (94.9%) > Ni5Zr/ZSM-5 (94.3%) > Ni3Zr/ZSM-5 (92.9%) > Ni/ZSM-5 (86.8%), which is consistent with the trend of carbon yield. Notably, the oxidation stability of CNFs is influenced by both their average diameter and defect density[39]. The derivative thermogravimetric (DTG) curves provide further insight into the oxidation kinetics (Figure 12(b)). The Ni/ZSM-5 catalyst exhibits the lowest onset weight loss temperature, followed by Ni5Zr/ZSM-5; in contrast, the Ni3Zr/ZSM-5 and Ni7Zr/ZSM-5 catalysts show higher and nearly identical onset and offset temperatures for weight loss. These differences in oxidation temperatures suggest variations in the average diameter and defect density of the CNFs produced by the different catalysts. Combined with the results of SEM and Raman spectroscopy, it can be concluded that the CNFs deposited on the Ni/ZSM-5 catalyst exhibit the smallest average diameter and the highest defect density. In comparison, the CNFs produced by the Ni7Zr/ZSM-5 catalyst exhibited a larger but more regular diameter, longer length, and fewer defects. Additionally, distinct differences are observed in the peak shapes and temperatures corresponding to the maximum weight loss rate in the DTG curves of the spent catalysts. The shape of peaks can reflect the thermal decomposition mechanism and reaction kinetics of the samples. The spent Ni/ZSM-5 and Ni5Zr/ZSM-5 catalysts exhibited sharp DTG peaks, indicating a fast oxidation reaction rate. In contrast, the Ni3Zr/ZSM-5 and Ni7Zr/ZSM-5 catalysts showed broader DTG peaks, which indicates a slower oxidation rate of the deposited carbon.

The temperatures at the maximum weight loss rate increased in the order: Ni/ZSM-5 < Ni5Zr/ZSM-5 < Ni3Zr/ZSM-5 < Ni7Zr/ZSM-5. This trend further confirms that the carbon on the Ni7Zr/ZSM-5 catalyst has the highest degree of graphitization and thermal stability.

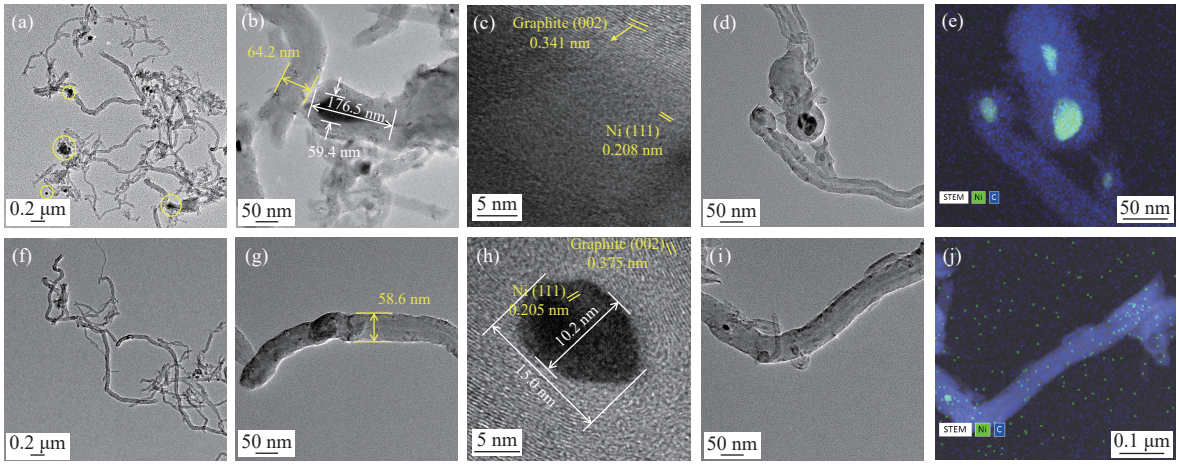


Fig. 11 TEM-EDX analysis for the spent (a)−(e) Ni/ZSM-5 and (f)−(j) Ni7Zr/ZSM-5 catalysts

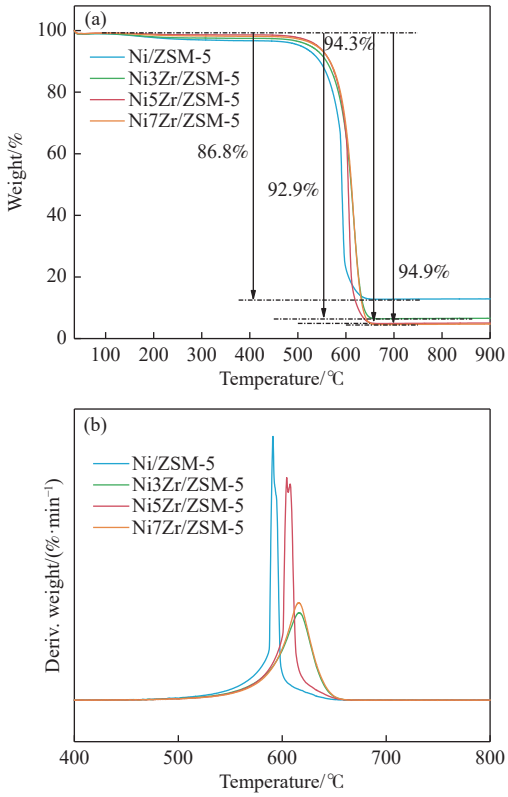


Fig. 12 (a) TG curves and (b) DTG profiles of the spent catalysts

3 Conclusion

In this work, a series of NixZr/ZSM-5 catalysts with different Zr loadings were prepared via the incipient wetness impregnation method. We investigated the role of ZrO_2 in regulating the structural properties and electronic effects of the catalysts, as well as its influence on catalytic methane decomposition performance. The evaluation results demonstrated that the stability of catalytic activity was significantly enhanced with the increase in Zr loading. Specifically, the Ni5Zr/ZSM-5 catalyst achieved a methane conversion of 68% under reaction conditions of 625 °C and a GHSV of 6000 mL/(h·g) and maintained catalytic activity for over 900 min with a carbon yield of 1927%. Characterization revealed that the introduction of ZrO_2 exerted a notable regulatory effect on the particle size and dispersion of Ni species. As the Zr content increased, the sizes of NiO on the calcined catalysts and Ni^0 on the reduced catalysts gradually decreased. The strong interaction between small NiO particles and the HZSM-5 support promoted the base-growth mode of carbon nanofibers. Furthermore, the electronic interactions between ZrO_2 and Ni species contribute to stabilizing the Ni active sites, thereby generating more active sites for CH_4 activation and enhancing the sintering resistance of the catalyst. The Characterization of TEM and Raman spectroscopy indicated that the CNFs produced over the Ni7Zr/ZSM-5 catalyst possessed a higher degree of graphitization with fewer defects. The incorporation of ZrO_2 facilitated the transition of the growth mode of CNFs from tip-growth to base-growth, significantly prolonging the catalyst lifetime and facilitating the production of high-quality CNFs.

Declaration of Competing Interest

The authors declare no conflict of interest.

References

[1] SINGH H, PARITOSH K, VIVEKANAND V, et al. Microorganism-assisted biohydrogen production and bioreactors[J]. Chem Eng Technol, 2023, 46(2): 204−217.

[2] LEVALLEY T L, RICHARD A R, FAN M. The progress in water gas shift and steam reforming hydrogen production technologies: A review[J]. Int J Hydrogen Energy, 2014, 39(30): 16983−17000.

[3] BAKENNE A, NUTTALL W, KAZANTZIS N. Sankey-diagram-based insights into the hydrogen economy of today[J]. Int J Hydrogen Energy, 2016, 41(19): 7744−7753.

[4] LI J Z, LÜ G X, LI K. Preparation of Ni/SiO_2 catalyst from monodisperse silica sol precursor for hydrogen production via methane cracking[J]. Nat Gas Chem Ind (C1 Chem Chem Eng), 2005, 30(1): 1−5.

[5] MAO Z Q, MAO Z M, YU H, et al. Hydrogen Production Process and Technology[M]. Beijing: Chemical Industry Press, 2018.

[6] AHMAD A, HAMDANI I R, SRINIVASAKANNAN C, et al. Catalytic cracking of methane to hydrogen and carbon: Scale-up perspective[J]. Int J Hydrogen Energy, 2024, 54: 1212−1230.

[7] WANG G, JIN Y, LIU G, et al. Production of hydrogen and nanocarbon from catalytic decomposition of methane over a $Ni-Fe/Al_2O_3$ catalyst[J]. Energy Fuels, 2013, 27(8): 4448−4456.

[8] PANGESTU M R G, MALAIBARI Z, MUHAMMAD A, et al. Comprehensive review on methane pyrolysis for sustainable hydrogen production[J]. Energy Fuels, 2024, 38(15): 13514−13538.

[9] GUTTA N, VELISOJU V K, TARDIO J, et al. CH_4 cracking over the Cu-Ni/Al-MCM-41 catalyst for the simultaneous production of H_2 and highly ordered graphitic carbon nanofibers[J]. Energy Fuels, 2019, 33(12): 12656−12665.

[10] YOON B S, YOUN J R, JUNG W G, et al. Catalytic methane decomposition using Ni supported on mesoporous SiO_2 catalyst: Ni position-dependent carbon yield change[J]. Appl Surf Sci, 2025, 692: 162731.

[11] HANTOKO D, KHAN W U, ALOMRAN A M, et al. The role of promoters in enhancing hydrogen production during catalytic decomposition of methane[J]. Catal Today, 2025, 453: 115259.

[12] RESHETENKO T V, AVDEEVA L B, ISMAGILOV Z R, et al. Carbon capacious $Ni-Cu-Al_2O_3$ catalysts for high-temperature methane decomposition[J]. Appl Catal A: Gen, 2003, 247(1): 51−63.

[13] HAMDAN M, HALAWY L, HIJAZI A, et al. Highly-stable

Ni-Zn catalyst on USY zeolite support for low temperature methane pyrolysis[J]. Int J Hydrogen Energy, 2024, 61: 840−850.

[14] BAYAT N, REZAEI M, MESHKANI F. Hydrogen and carbon nanofibers synthesis by methane decomposition over Ni-Pd/Al_2O_3 catalyst[J]. Int J Hydrogen Energy, 2016, 41(12): 5494−5504.

[15] KARIMI S, BIBAK F, MESHKANI F, et al. Promotional roles of second metals in catalyzing methane decomposition over the Ni-based catalysts for hydrogen production: A critical review[J]. Int J Hydrogen Energy, 2021, 46(39): 20435−20480.

[16] LIU P, LU J C, CHEN D K, et al. Research progress on hydrogen production by thermal catalytic cracking of methane over carbonaceous and metal catalysts[J]. J Mol Catal (China), 2016, 30(5): 480−495.

[17] WANG D, ZHANG J, SUN J, et al. Effect of metal additives on the catalytic performance of Ni/Al_2O_3 catalyst in thermocatalytic decomposition of methane[J]. Int J Hydrogen Energy, 2019, 44(14): 7205−7215.

[18] WANG W, WANG H, YANG Y, et al. Ni-SiO_2 and Ni-Fe-SiO_2 catalysts for methane decomposition to prepare hydrogen and carbon filaments[J]. Int J Hydrogen Energy, 2012, 37(11): 9058−9066.

[19] LÜ Y, DING Y J, LIN L W. Modification of Ni-based catalysts for methane decomposition to hydrogen and carbon nanofibers[J]. Petrochem Technol, 2004, 33(S1): 243−245.

[20] KOSARI M, PORTILLO S B, XI S, et al. Zr-promoted Ni nanoparticles in mesoporous silica spheres (NiZr/*m*SiO_2) for catalytic decomposition of methane[J]. Chem Eng J, 2025, 507: 160328.

[21] CHEIN R Y, OU C C. Experimental study on finding stable catalytic methane decomposition for hydrogen production[J]. Int J Hydrogen Energy, 2025, 139: 946−955.

[22] LI J, DONG L, XIONG L, et al. High-loaded NiCuSiO_2 catalysts for methane decomposition to prepare hydrogen and carbon filaments[J]. Int J Hydrogen Energy, 2016, 41(28): 12038−12048.

[23] KARAMINEJAD M, GOLHOSSEINI R, MESHKANI F, et al. Insight into the moderate interaction between the metal and support and reinforcing of Ni/SiO_2-based catalysts efficiency with the manganese integration in thermal catalytic methane decomposition[J]. Energy Convers Manage, 2025, 323: 119229.

[24] SING K S W. Reporting physisorption data for gas/solid systems with special reference to the determination of surface area and porosity (Recommendations 1984)[J]. Pure Appl Chem, 1985, 57(4): 603−619.

[25] LI J, FU Z H, FU H, et al. Mn-doped Ni/ZSM-5 for plasma-catalytic partial reforming of methane to hydrogen[J]. Ind Catal, 2024, 32(2): 54−58.

[26] RAHMANI F, HAGHIGHI M, VAFAEIAN Y, et al. Hydrogen production via CO_2 reforming of methane over ZrO_2-doped Ni/ZSM-5 nanostructured catalyst prepared by ultrasound assisted sequential impregnation method[J]. J Power Sources, 2014, 272: 816−827.

[27] SHEN Y, LUA A C. Synthesis of Ni and Ni-Cu supported on carbon nanotubes for hydrogen and carbon production by catalytic decomposition of methane[J]. Appl Catal B: Environ, 2015, 164: 61−69.

[28] JONES R D, BARTHOLOMEW C H. Improved flow technique for measurement of hydrogen chemisorption on metal catalysts[J]. Appl Catal, 1988, 39: 77−88.

[29] SABARISH R, UNNIKRISHNAN G. Synthesis, characterization and catalytic activity of hierarchical ZSM-5 templated by carboxymethyl cellulose[J]. Powder Technol, 2017, 320: 412−419.

[30] DAI L, WANG Y, LIU Y, et al. Catalytic fast pyrolysis of torrefied corn cob to aromatic hydrocarbons over Ni-modified hierarchical ZSM-5 catalyst[J]. Bioresour Technol, 2019, 272: 407−414.

[31] HONGMANOROM P, ASHOK J, DAS S, et al. Zr-Ce-incorporated Ni/SBA-15 catalyst for high-temperature water gas shift reaction: Methane suppression by incorporated Zr and Ce[J]. J Catal, 2020, 387: 47−61.

[32] SUN M, XIA J, WANG H, et al. An efficient NixZryO catalyst for hydrogenation of bio-derived methyl levulinate to γ-valerolactone in water under low hydrogen pressure[J]. Appl Catal B: Environ, 2018, 227: 488−498.

[33] PHICHAIRATANAPHONG O, TEEPAKAKORN P, POO-ARPORN Y, et al. Infiltrate mesoporous silica-aluminosilicate structure improves hydrogen production via methane decomposition over a nickel-based catalyst[J]. Ind Eng Chem Res, 2021, 60(12): 4562−4574.

[34] IVLEVA N P, MESSERER A, YANG X, et al. Raman microspectroscopic analysis of changes in the chemical structure and reactivity of soot in a diesel exhaust aftertreatment mode system[J]. Environ Sci Technol, 2007, 41(10): 3702−3707.

[35] QIAN J, LI H, SUN D, et al. Tuning Mg-Fe-O solid solutions towards optimized exsolution of active sites for thermal catalytic decomposition of methane[J]. Chem Eng J, 2024, 497: 154595.

[36] LAN M C, SHEN B X, WANG J Q, et al. Performance of Ni-based catalysts supported on different activated carbons for pyrolysis of waste plastics to carbon nanotubes[J]. J Fuel Chem Technol, 2019, 47(11): 1313−1319.

[37] DONPHAI W, PHICHAIRATANAPHONG O, KLYSUBUN W, et al. Hydrogen and carbon allotrope production through methane cracking over Ni/bimodal porous silica catalyst: Effect of nickel precursor[J]. Int J Hydrogen Energy, 2018, 43(48): 21798−21809.

[38] TORRES D, PINILLA J L, LÁZARO M J, et al. Hydrogen and multiwall carbon nanotubes production by catalytic decomposition of methane: Thermogravimetric analysis and scaling-up of Fe-Mo catalysts[J]. Int J Hydrogen Energy, 2014, 39(8): 3698−3709.

[39] CHEN C M, DAI Y M, HUANG J G, et al. Intermetallic catalyst for carbon nanotubes (CNTs) growth by thermal chemical vapor deposition method[J]. Carbon, 2006, 44(9): 1808−1820.

Zr 对负载型 Ni 基催化剂电子和结构的调变及其对甲烷催化裂解反应的影响

刘　璐，任申勇*，姚成树，申宝剑，徐春明

（中国石油大学 (北京) 化学工程与环境学院 重质油全国重点实验室 CNPC 催化重点实验室, 北京 102249）

摘　要: 甲烷催化裂解制备高纯氢气及高附加值碳纳米材料展现出了良好的发展潜力，有望在未来实现显著的经济价值，但对该反应兼具高活性和长寿命的催化剂一直是研究的难点。通过调控催化剂的结构及电子状态优化反应性能是有效的策略。本工作采用等体积浸渍法制备了一系列 NixZr/ZSM-5 催化剂，考察了 Zr 负载量对催化剂性质和反应性能的影响。使用低温 N_2 吸附-脱附、XRD、SEM、H_2-TPR 和 XPS 等表征方法对还原前后的催化剂进行分析。结果表明，Zr 的加入显著提高了催化剂的比表面积并降低金属颗粒的尺寸，小颗粒的 Ni^0 颗粒可进入 HZSM-5 载体孔道内，同时 Ni 与 ZrO_2 间的电子效应可促进金属-载体间相互作用显著增强。当 Zr 负载量为 5% 时催化剂表现出了最佳的催化性能，在 625 ℃ 最高甲烷转化率为 68% 且可保持 900 min 活性无明显下降，其炭产率可达 1927%。继续提高 Zr 添加量，催化剂性能提升有限。通过 TEM、Raman、TGA 对反应后催化剂及炭产物进行表征发现，助剂 ZrO_2 的引入可以减少金属烧结，促进碳纳米纤维的生长模式由顶端生长转变为基底生长，从而使得催化剂可维持较长时间的活性。

关键词: 助剂 ZrO_2; Ni/HZSM-5; 甲烷催化裂解; 碳纳米纤维

中图分类号: TQ116.2　　**文献标识码:** A

作者简介:



刘璐(2000)，博士研究生，研究方向为甲烷裂解制氢，liulu_ll2021@163.com。



任申勇(1977)，博士，副教授，研究方向为无机多孔材料及油气转化催化剂的制备与应用，shenyong@cup.edu.cn。